Dynamic organization of cortical actin filaments during the ooplasmic segregation of ascidian *Ciona* eggs

Hirokazu Ishii[†,‡] and Tomomi Tani[§,*]
Eugene Bell Center for Regenerative Biology and Tissue Engineering, Marine Biological Laboratory, Woods Hole, MA 02543

ABSTRACT Spatial reorganization of cytoplasm in zygotic cells is critically important for establishing the body plans of many animal species. In ascidian zygotes, maternal determinants (mRNAs) are first transported to the vegetal pole a few minutes after fertilization and then to the future posterior side of the zygotes in a later phase of cytoplasmic reorganization, before the first cell division. Here, by using a novel fluorescence polarization microscope that reports the position and the orientation of fluorescently labeled proteins in living cells, we mapped the local alignments and the time-dependent changes of cortical actin networks in *Ciona* eggs. The initial cytoplasmic reorganization started with the contraction of vegetal hemisphere approximately 20 s after the fertilization-induced $[Ca^{2+}]$ increase. Timing of the vegetal contraction was consistent with the emergence of highly aligned actin filaments at the cell cortex of the vegetal hemisphere, which ran perpendicular to the animal–vegetal axis. We propose that the cytoplasmic reorganization is initiated by the local contraction of laterally aligned cortical actomyosin in the vegetal hemisphere, which in turn generates the directional movement of cytoplasm within the whole egg.

INTRODUCTION

During early development of many animal species, including vertebrates, redistributions of cytoplasmic maternal substances in zygotes play important roles in the determination of body axes in the embryos (Lyczak *et al.*, 2002; Pelegri, 2003; Weaver, 2004; Ma *et al.*, 2016; Nishikata *et al.*, 2019). The ascidian zygotes show drastic reorganization of cytoplasm from the time before the first cell division (Sardet *et al.*, 2007; Makabe and Nishida, 2012), which has been traditionally called ooplasmic segregation. The initial cytoplasmic reorganization occurs immediately after the fertilization caused by the contraction of cortical actomyosin network (Jeffery and Meier, 1983; Jeffery, 1984; Sawada, 1983; Sawada and Osanai, 1984, 1985). The following reorganization of cytoplasm is driven by multiple microtubule systems that include sperm asters (Sawada and Schatten, 1988; Chiba *et al.*, 1999; Ishii *et al.*, 2017; Goto *et al.*, 2019). Importantly, these cytoplasmic movements are critically important for the establishment of the body axes of the ascidian embryo during development (Nishida, 2005; Makabe and Nishida, 2012). The interplay of these two cytoskeletal dynamics helps redistribution of the maternal mRNAs called *postplasmic/PEM* RNAs, which include the muscle determinant, *macho-1* (Nishida, 2005; Makabe and Nishida, 2012). These maternal mRNAs regulate gene expressions for cell-specific differentiations, cell polarity, and cell division planes in the blastomeres (Sardet, 2003; Prodon *et al.*, 2007).

Ooplasmic segregation in ascidian eggs is triggered by fertilization. The first phase is initiated immediately after the fusion of the sperm to the egg, in which the myoplasm, a mitochondria-rich cytoplasmic domain containing *postplasmic/PEM* RNAs, begins to move toward the vegetal pole. Electron microscopic studies have suggested that the contraction of the cortical domain (plasma

membrane lamina; PML) drives the first phase of ooplasmic segregation (Jeffery and Meier, 1983; Jeffery, 1984). Since this domain was stained by fluorescent phalloidin (Jeffery and Meier, 1983; Sawada and Osanai, 1985; Chiba et al., 1999), the actin cytoskeleton was likely to be the major component of this domain. Inhibitor studies had suggested the involvement of the actin cytoskeleton in the movements (Zalokar, 1974; Reverberi, 1975; Sawada and Osanai, 1985; Chiba et al., 1999; Takatori et al., 2015). Jeffery and Meier (1983; also see Jeffery, 1984; and Sawada, 1983) had proposed similar models independently for the mechanism of ooplasmic segregation in ascidian eggs. These models are based on the contraction of actomyosin networks that spread over the egg cortex. Their models proposed that the actin-rich cell cortex is connected to the egg plasma membrane and to inner cytoplasm. The initial event of ooplasmic segregation starts with the contraction of the basket-shaped, actin-rich cell cortex toward the vegetal pole. The contraction of the actin-rich cortex to the vegetal pole produces the force that displaces the vegetal cytoplasm to the animal hemisphere. The updated models also support the models of Jeffery and Meier (1983) and Sawada (1983) (Prodon et al., 2007; Sardet et al., 2007; Makabe and Nishida, 2012) and add more precise explanations for the reorganization patterns of maternal factors such as mitochondria, the cortical endoplasmic reticulum (cER), and postplasmic/PEM RNAs during ooplasmic segregation.

The mechanism of how actomyosin contractility leads to the directional movement of maternal substances remains an unsolved problem. In this study, we have tackled this problem by using two advanced light microscopy techniques. One is selective plane illumination microscopy (SPIM) (Huisken and Stainier, 2009) to visualize the morphological change and cytoplasmic movement initiated by the fertilization-induced Ca^{2+} wave (Dumollard et al., 2004). SPIM allowed us to observe Ca^{2+} dynamics and the following cytoplasmic movements in the whole Ciona egg as large as 140 μm in diameter with a high signal-to-noise ratio, revealing the local differences of Ca^{2+} dynamics and cytoplasmic movement of the fertilized Ciona egg in the vegetal hemisphere and those in the animal hemispheres in live eggs. Another is the polarized fluorescence microscope (instantaneous FluoPolScope) that we have developed for observing the orientation of fluorescently labeled biomolecules in live cells (Mehta et al., 2016; Nordenfelt et al., 2017; Swaminathan et al., 2017; Altartouri et al., 2019; Nakai et al., 2019). The alignment of cortical actomyosin filaments is the key event for determining the orientation of force production in a variety of cell movements such as cell division and cell migration. The observation of cortical F-actin alignments is a powerful approach to explore the mechanisms of ooplasmic segregation. However, this trial has been hampered by the spatial resolution of light microscopy in the context of live cell imaging. The instantaneous FluoPolScope reports alignment of molecular assemblies with single-molecule sensitivity (Mehta et al., 2016). On the basis of correlative imaging of cytoplasmic movement, intracellular [Ca^{2+}], and the spatial organization of actin filaments in fertilized Ciona eggs, we found distinct spatial organizations of the actin cytoskeleton and their dynamics at the vegetal hemisphere and the animal hemisphere of Ciona eggs during the cytoplasmic reorganization. We will update the mechanisms of the spatial organization of cortical actomyosin for the first ooplasmic segregation in ascidian eggs.

RESULTS

Optical dissection of cytoplasmic reorganization in Ciona eggs by using SPIM

We examined the dynamics of cytoplasmic reorganization in fertilized Ciona eggs by using a new imaging tool, the SPIM. As shown in Figure 1A, fertilization induced an increase in intracellular [Ca^{2+}] and the overall morphological change of the egg in parallel with the translocation of the autofluorescent myoplasm (Deno, 1987; Nishikata et al., 1987) toward the vegetal pole. The myoplasm, which was observed with 488 nm laser light sheet illumination and a green emission filter (529/24 nm), was distributed over the cell cortex of the vegetal hemisphere of Ciona eggs. The domain is composed of a mitochondria-rich inner layer and a cER domain with postplasmic/PEM RNAs (Sardet et al., 2007). The movement of the myoplasm resulted in the formation of a dense layer of myoplasm at the vegetal pole (Sardet et al., 1989). Together with the myoplasmic contraction, we observed a series of deformations of the fertilized egg. These morphological changes were associated with the elevation of intracellular [Ca^{2+}] (Speksnijder et al., 1990; Roegiers et al., 1995), as is shown in the top panel of Figure 1B. After the elevation of [Ca^{2+}], the deformation of the egg started with a transient extension of the egg along the animal–vegetal (A–V) axis for less than 2 min (aspect ratio >1), followed by a long-lasting compression to the equatorial plane (aspect ratio <1) (bottom panel of Figure 1B). The onset of the egg extension was observed ~20 s after the onset the [Ca^{2+}] increase. The compression of the egg started in the middle of the slow decay phase of the fertilization-induced Ca^{2+} wave.

As shown in Figure 1, C and D, and Supplemental Movie S1, we monitored fertilization-triggered cortical movements in both vegetal and animal hemispheres by tracking the autofluorescent granules in the myoplasm and 100-nm-diameter fluorescent polystyrene beads (microsphere; ex: 580 nm/em: 605 nm; Molecular Probes) that had been microinjected into the cytoplasm of unfertilized Ciona eggs. We confirmed in separate observations that the autofluorescent granules were specifically stained with a fluorescent mitochondria marker, MitoTracker Red CMXRos (see Supplemental Figure S1). In two kymographs along the circumference of the egg cell cortex (Figure 1, C and D), the autofluorescent granules at the vegetal hemisphere and the microinjected beads at the animal hemisphere all moved toward the vegetal pole along the cortex. We also observed a short, directional movement of cytoplasm with polystyrene beads in the middle of the eggs, from the vegetal pole to the animal pole direction (unpublished data). We found that the contraction of myoplasm at the vegetal hemisphere preceded the cortical movements at the animal hemisphere. In Figure 1D, there was a short latency at the start of polystyrene bead movement along the cortex at the animal hemisphere. Tracking analysis of autofluorescent granules at the vegetal hemisphere (Figure 1E) and the polystyrene beads at the animal hemisphere (Figure 1F) revealed that the initiation of cortical movement at the animal hemisphere started approximately 5–20 s after the onset of the contraction of myoplasm at the vegetal hemisphere. The total distance of translocation of microinjected beads along the cortex of the animal hemisphere was approximately 40–60 μm (Figure 1F), whereas the myoplasmic movement from the equator to the vegetal pole was approximately 30 μm (Figure 1E). The speeds at the onset of their movements were similar (58.5 μm min^{-1} for myoplasm and 49.3 μm min^{-1} for beads at the animal hemisphere) and gradually slowed down within 4–5 min. These time correlations of cytoplasmic movements suggested the idea that the initiation of myoplasmic contraction at the vegetal hemisphere leads the first phase of ooplasmic segregation in ascidian zygotes, as proposed in the models of Jeffery and Meier (1983) and Sawada (1983).

The direction of intracellular Ca^{2+} waves correlates with the cell polarity of fertilized Ciona eggs

We observed the correlation of Ca^{2+} waves with actomyosin-driven ooplasmic segregation and egg morphology changes (Supplemental
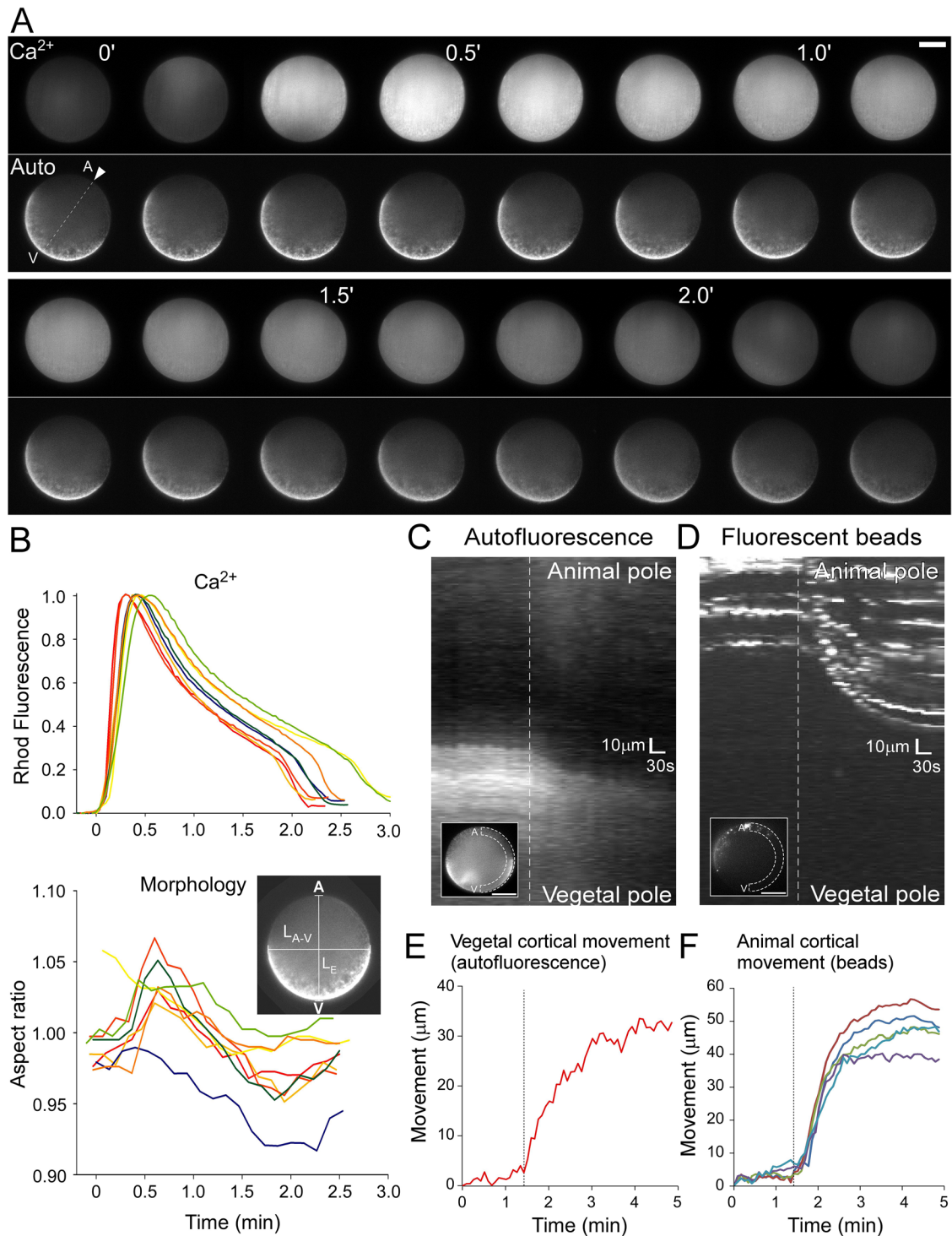
FIGURE 1: Fertilization-induced intracellular Ca²⁺ wave and the following cytoplasmic reorganization in the *C. intestinalis* egg. (A) Time series fluorescence images of Ca²⁺ indicator Rhod-dextran (top lane) and autofluorescence (bottom lane) in fertilized *Ciona* eggs observed with SPIM. A white arrow in the first autofluorescence image indicates the position of the meiotic spindle as a landmark of the animal pole. A and V indicate the positions of the animal pole and the vegetal pole, respectively. The numbers at the top right of selected images indicate the time (in minutes) after the start of [Ca²⁺] elevation. Bar, 50 µm. (B) Fertilization-induced [Ca²⁺] changes (top panel) and the morphology changes (bottom panel) observed in nine preparations are plotted against time. Fertilization-induced [Ca²⁺] changes are shown as the normalized fluorescence intensity changes of Rhod-dextran. The morphological changes are expressed as a time series of change in the aspect ratio, the value derived from the length between the animal and the vegetal poles (L_{A-V}) divided by the equatorial radius (L_E). Time zero for each data set is adjusted by the initial onset of Ca²⁺ elevation. (C, D) Kymographs of autofluorescent granules (mitochondria) in the myoplasm (C) and 100 nm fluorescent beads microinjected into the cytoplasm (D), both moving along the cortex of the *Ciona* egg after fertilization. Averaged fluorescence intensity profiles along the curved areas enclosed by white broken lines (inset) were aligned from left to

Movie S2). Multiple Ca^{2+} waves with different origins occurred after fertilization. The first, fertilization induced, long-lasting large Ca^{2+} wave originated from a small area (Figure 2A, top lane) that had been reported as the point of sperm–egg fusion (Speksnijder *et al.*, 1990; Roegiers *et al.*, 1995). To enhance the wavefront images of the traveling Ca^{2+} waves observed with SPIM, we processed the series of time-derivative Rhod-dextran fluorescence images by subtracting the consecutive images (taken every 2 s) one after another (Figure 2A, middle lane). Consistent with previous reports (Speksnijder *et al.*, 1990; McDougall and Sardet, 1995), the speed of propagation of the fertilization-induced Ca^{2+} wave was approximately 7.5 µm s^{-1}. It is worth noting that in the SPIM images in Figure 2A, the speed of Ca^{2+} wave propagation along the cell cortex was faster than that of the wave that ran in the middle of the cytoplasm; the shape of the wavefront was convex in the beginning, then it was straight in the middle, and then it changed to concave in the end of the traveling wave. Similar observations were reported in ascidian eggs by using confocal microscopy and simulation models (Dupont and Dumollard, 2004).

A series of short repetitive Ca^{2+} waves followed the initial fertilization-induced Ca^{2+} wave (Figure 2C), which have been called Ca^{2+} pacemaker waves (Speksnijder *et al.*, 1990; Roegiers *et al.*, 1995; Dumollard and Sardet, 2001). In our observations, these repetitive waves originated from the vegetal hemisphere, but the initial wave was often observed not as a small point, but as a broad cup-shape area as shown in the time-derivative images (Figure 2C, middle lane, *t* = 2′46″). The location of this cup-shape Ca^{2+} distribution was consistent with that of the autofluorescent myoplasm (Figure 2C, bottom lane), indicating that pacemaker Ca^{2+} waves originated from the subcellular structures that associated with myoplasm. The propagation rate of the pacemaker Ca^{2+} waves was approximately 25–50 µm s^{-1}, which was much faster than that of the fertilization-induced Ca^{2+} wave.

SPIM imaging showed not only the wave of [Ca^{2+}] increase but also a wave of decreasing [Ca^{2+}], which we called the "Ca^{2+}-sequestering wave." As far as we know, this is the first time a propagating wave of [Ca^{2+}] decrease is reported. The Ca^{2+}-sequestering waves followed the initial fertilization Ca^{2+} wave as is clearly observed in Figure 2B and after the following Ca^{2+} pacemaker waves (unpublished data). In other words, we observed Ca^{2+}-sequestering waves every time after [Ca^{2+}] increases. Interestingly, the origins of these Ca^{2+}-sequestering waves were consistently from the animal pole. The Ca^{2+}-sequestering wave was not a back of the propagating Ca^{2+} wave when the wave passes by, as in many cases we observed that the propagating direction of the Ca^{2+} wave was different from that of the Ca^{2+}-sequestering wave. The velocity of the Ca^{2+}-sequestering waves was 5–6 µm s^{-1}, which was slightly faster than that of the first Ca^{2+} wave and much slower than that of the Ca^{2+} pacemaker waves. We did not detect any difference between the velocities of Ca^{2+}-sequestering waves observed after the fertilization-induced Ca^{2+} wave and those observed after pacemaker Ca^{2+} waves. In Figure 2D, we plotted the propagating directions of the first Ca^{2+} waves, Ca^{2+} pacemaker waves, and Ca^{2+}-sequestering waves with respect to the A–V axis. The origins of the fertilization-induced Ca^{2+} waves spread all over the surface of the *Ciona* egg,

which was not consistent with the observations using a different species of ascidian, *Phallusia*, in which the origin of the first Ca^{2+} waves was around the animal pole (Speksnijder *et al.*, 1990; Roegiers *et al.*, 1995). In the following Ca^{2+} pacemaker waves, approximately 70% (nine of 13 waves) traveled to the animal pole side. In the Ca^{2+}-sequestering waves, all waves we observed (13 waves) propagated along the A–V axis from the animal pole to the vegetal pole, regardless of the origins and the propagation directions of the preceding [Ca^{2+}] raises. On the basis of these observations, in later experiments we used the direction of Ca^{2+}-sequestering waves as a reference to identify the A–V axis of fertilized *Ciona* eggs.

It is worth noting that the autofluorescence of *Ciona* eggs, observed through the 529/24 nm emission filter, oscillated along with the Ca^{2+} waves (Figure 2E). These changes could be observed in the autofluorescence signal at the myoplasm as well as at the cytosol of the fertilized eggs. Interestingly, the changes in the autofluorescence correlated only with the Ca^{2+} pacemaker waves, but not with the first fertilization-induced Ca^{2+} wave. At the onset of the fertilization-induced increase in [Ca^{2+}] (Figure 2E, vertical broken line *a*), we did not observe the increase of autofluorescence intensity, but we observed the oscillation of autofluorescence that was correlated with the Ca^{2+} oscillation. Similar autofluorescence changes that correlated with changes in [Ca^{2+}] had been reported in fertilized mouse eggs (Dumollard *et al.*, 2004).

Correlative imaging of intracellular [Ca^{2+}], cortical actin dynamics, and membrane contraction of fertilized *Ciona* eggs observed with total internal reflection fluorescence microscopy

Previous studies (Jeffery and Meier, 1983; Jeffery, 1984; Sawada and Osanai, 1984, 1985) had demonstrated that the first phase of ooplasmic segregation and egg morphology changes were closely related to the contractility of actomyosin at the cell cortex of ascidian eggs. Based on fluorescence imaging of fixed cells by fluorescent phalloidin labeling (Jeffery and Meier, 1983; Sawada, 1983; Chiba *et al.*, 1999) or by isolated cortex (Sardet *et al.*, 1992; Prodon *et al.*, 2005), the actin cytoskeleton seemed to exist very close to the cortical membrane. But the mechanisms of the actomyosin system that translocate the maternal substances to the vegetal pole were not clear in the context of live cell imaging. We have studied actin cytoskeleton dynamics in fertilized *Ciona* eggs by using total internal reflection fluorescence microscopy (TIRFM). We microinjected Alexa Fluor 488 phalloidin (AF488-phalloidin; final concentration, ~10 nM; see *Materials and Methods* for details) and Rhod-dextran (final concentration, 50–500 nM; see *Materials and Methods* for details) into unfertilized *Ciona* eggs. The eggs with AF488-phalloidin and Rhod-dextran were placed on cleaned glass coverslips and were observed with TIRFM. The observed area was approximately 40–50 µm in diameter, which was one third of the average diameter of *Ciona* eggs (Figure 3A). As we have described for SPIM imaging, autofluorescence images could be observed with the fluorescence imaging setting for observing AF488-phalloidin. We compared the fluorescence intensities of *Ciona* eggs before and after microinjecting AF488-phalloidin. Autofluorescence accounted for roughly 1/5 of the observed intensity at 529 nm.

---

right to create the kymographs. The top of the kymograph represents the animal pole (A in the insets), and the bottom represents the vegetal pole (V in the insets). Vertical white broken lines in C and D represent the time when the movement of autofluorescent granules in the myoplasm started. (E, F) Trajectories of autofluorescent granules in myoplasm (E) and 100 nm fluorescent beads (F) that moved along the cell cortex of the *Ciona* egg after fertilization. Vertical black lines in the graphs represent the time when the movement of autofluorescent granules starts. The times (abscissa in minutes) are measured after the onset of [Ca^{2+}] elevation.
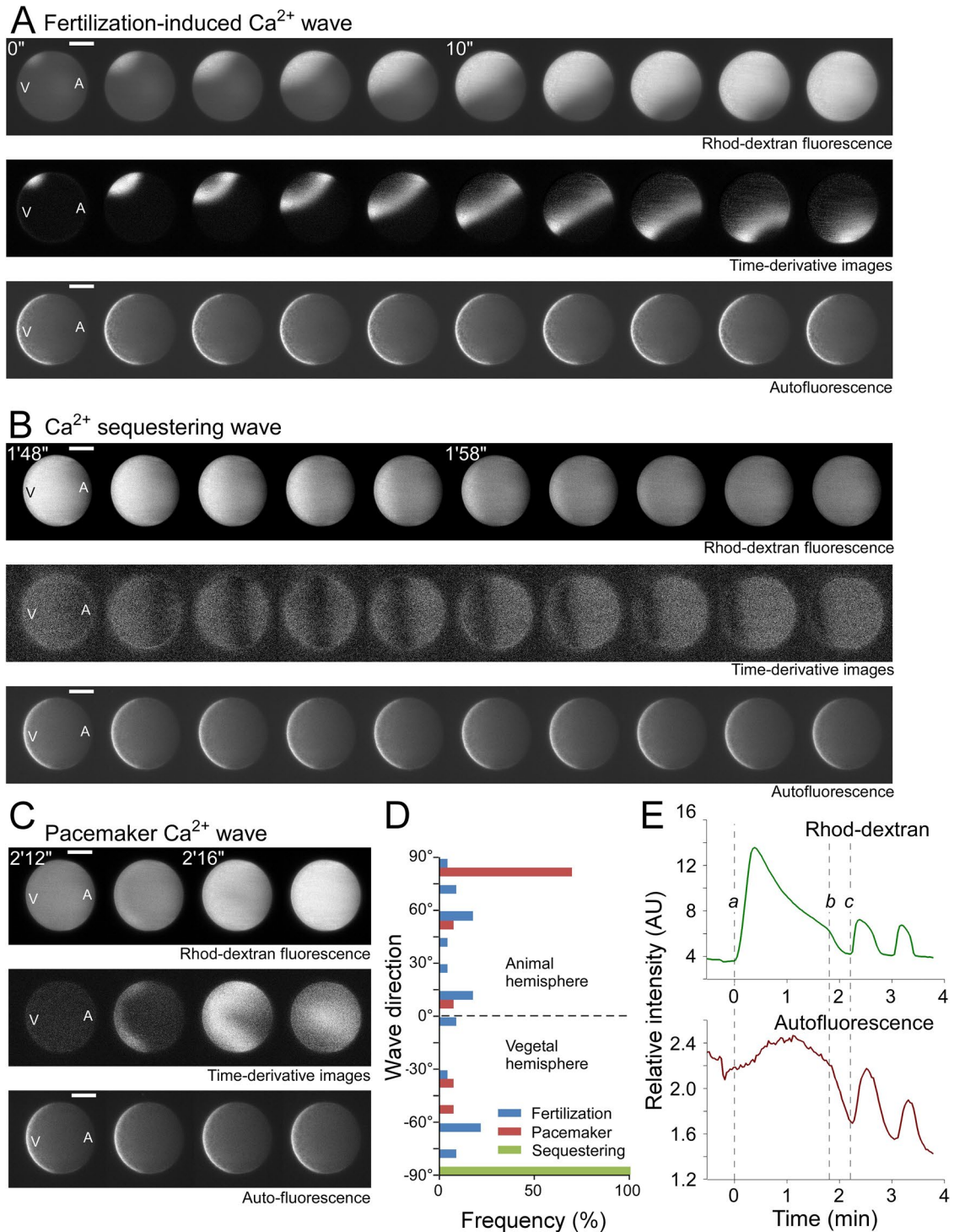
FIGURE 2: The origins and propagation directions of intracellular Ca^{2+} waves in the fertilized *C. intestinalis* egg. (A) Top lane: Time series of Rhod-dextran fluorescence images showing the propagation of the fertilization-induced Ca^{2+} wave. The images were taken every 2 s. Times after the beginning of initial $[Ca^{2+}]$ elevation are shown at the top left of selected images. Middle lane: Time derivative images of Rhod-dextran fluorescence obtained by subtracting two consecutive images in the top lane, one after the other. Bottom lane: Time series of autofluorescence images during the first fertilization-induced Ca^{2+} wave. A and V indicate the positions of the animal pole and the vegetal pole, respectively. Bars, 50 μm. (B) Top lane: Time series of Rhod-dextran fluorescence images showing the propagation of the Ca^{2+}-sequestering wave. Times after the beginning of initial fertilization-induced Ca^{2+} elevation are shown at the top left of selected images. Middle lane: Time derivative images of Rhod-dextran fluorescence that enhance the wavefront of the Ca^{2+}-sequestering wave. Bottom lane: Autofluorescence images during a passage of the Ca^{2+}-sequestering wave. A and V indicate the positions of the animal pole and the vegetal pole, respectively. Bars, 50 μm. (C) Top lane: Time series of Rhod-dextran fluorescence images showing a propagation of the pacemaker Ca^{2+} wave. Times after the beginning of initial fertilization-induced $[Ca^{2+}]$ elevation are shown at the top left of selected images. Middle lane: Time derivative
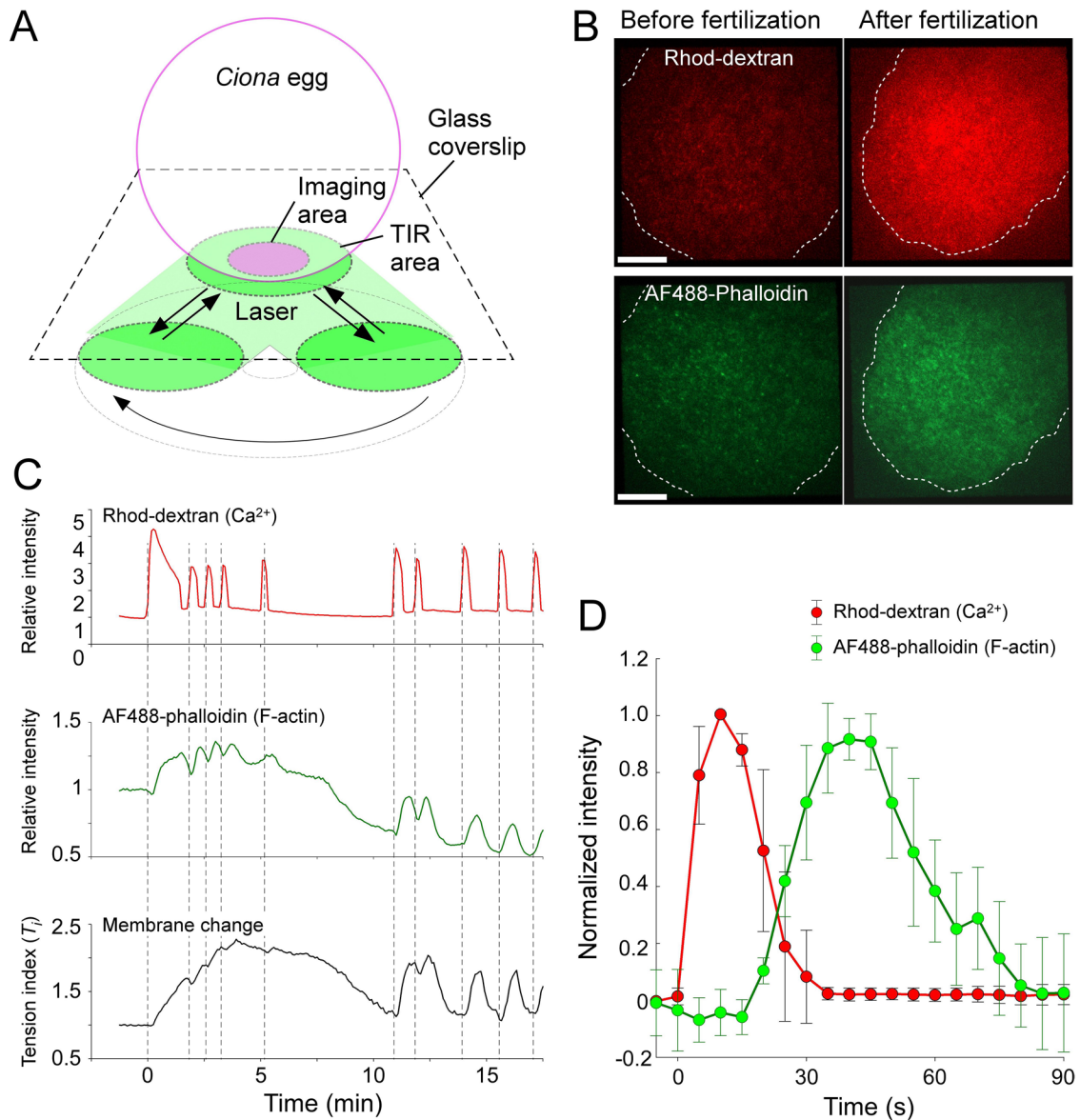
FIGURE 3: Correlative imaging of [Ca²⁺], F-actin dynamics, and membrane changes in the fertilized *C. intestinalis* egg. (A) Schematic drawing showing the imaging area of the *Ciona* egg placed on a glass coverslip for the TIRFM. (B) TIRFM images of Rhod-dextran (top panels) and AF488-phalloidin (bottom panels) before (left) and 30 s after (right) the onset of the first [Ca²⁺] elevation. Bars, 10 µm. (C) Time series of fluorescence intensity changes in Rhod-dextran for Ca²⁺ concentration (top), AF488-phalloidin for F-actin (middle), and the membrane tension index derived from the equations of Hiramoto (1976) for estimating the membrane tension of round cells (bottom). Time 0 is the onset of the first [Ca²⁺] elevation. (D) The normalized and averaged [Ca²⁺] changes and the following changes of F-actin. The values 5 s before the onset of the [Ca²⁺] increase and the peak values of the Ca²⁺ wave were used for normalizing the absolute values. The center of each circle represents the mean value, and the length of the vertical line represents the SD. Six waveforms of the pacemaker wave were used for averaging the normalized values.

images of Rhod-dextran fluorescence during the propagation of the pacemaker Ca²⁺ wave. Bottom lane: Autofluorescence images during the propagation of the pacemaker Ca²⁺ wave. A and V indicate the positions of the animal pole and the vegetal pole, respectively. Bars, 50 µm. (D) Histograms showing the directions of wave propagations in the first fertilization-induced Ca²⁺ wave (blue), the pacemaker waves (red), and the sequestering waves (green). Ninety degrees (90°) represents the wave direction toward the animal pole and –90° represents the direction toward the vegetal pole. Numbers of eggs examined: 23 for the fertilization-induced wave, 13 for pacemaker waves, and 13 for sequestering waves. (E) Oscillation of intracellular [Ca²⁺] monitored by Rhod-dextran fluorescence (top trace) and that of autofluorescence (bottom trace). Time is measured after the beginning of initial fertilization-induced [Ca²⁺] elevation. Timings indicated by *a*, *b*, and *c* correspond to the timings of the first frames of panels A, B, and C, respectively.

Upon fertilization, we observed increases in the fluorescence intensities of both Rhod-dextran and AF488-phalloidin in the *Ciona* egg cortex adjacent to the glass coverslip (Figure 3B). Monitoring these fluorescence changes allowed us to correlate [Ca^{2+}] and F-actin assembly that was labeled with AF488-phalloidin. Among 14 correlative observations, one set of [Ca^{2+}] and F-actin changes as well as the membrane area change are shown in Figure 3C and Supplemental Movie S3 as a typical example. Consistently with a previous report (Dumollard *et al.*, 2004) and with our SPIM observations (Figures 1 and 2), the fertilized egg showed an initial, long-lasting (~2 min) Ca^{2+} wave, which was followed by multiple pacemaker waves that were observed within 5–6 min from the first [Ca^{2+}] elevation. In AF488-phalloidin fluorescence signals, we observed a large transient increase followed by small fluctuations after fertilization. During the period of pacemaker wave propagation, we found that there was a delay between the increase of [Ca^{2+}] and that of the following AF488-phalloidin fluorescence (Figure 3C; vertical lines indicate the onset times for the increases in [Ca^{2+}]). The normalized and averaged changes of six pacemaker Ca^{2+} waves and those of the corresponding AF488-phalloidin fluorescence revealed that the AF488-phalloidin fluorescence intensity reached its maximum value approximately 30 s after the maximum increase of [Ca^{2+}] (Figure 3D). Thus, the transient changes of AF488-phalloidin fluorescence followed the transient [Ca^{2+}] changes, with a delay of approximately 30 s for each period after the [Ca^{2+}] change.

We observed periodical changes in the contact surface of *Ciona* eggs with the glass coverslip. These changes might reflect the cortical tension of the eggs. To estimate the change in cortical tension, we employed an equation by Hiramoto (1976) for estimating the cortical tension of sea urchin eggs placed on a glass surface. In Hiramoto's estimation, tension at the membrane (T_m) of a spherical egg placed on a flat substrate is proportional to the inverse of the area attached to the substrate,

$$T_m = \frac{2R_0^4 \; (r-s)g}{3R_m^2}$$

where R_o is the radius of the egg at the largest optical section, R_m is the radius of membrane area attached to the substrate, r is the density of the egg, s is the density of seawater, and g is the gravity constant. At the bottom of Figure 3C, we plotted the time-dependent change of the inverse of the membrane area attached to the glass coverslip as membrane tension index T_i to show the relative changes in tension at the membrane while [Ca^{2+}] and the amount of F-actin were changing. T_i changed simultaneously with the increase of Rhod-dextran and AF488-phalloidin fluorescence, suggesting that Ca^{2+}-induced actomyosin contraction induced the membrane contraction at the cell surface. Similarly to the changes in AF488-phalloidin, the onset of the membrane tension increase was approximately 30 s after the increase of [Ca^{2+}], which was consistent with the delay in the morphological change after the [Ca^{2+}] increase, as we observed in SPIM imaging (Figure 1B).

Approximately 8–10 min after the onset of the first Ca^{2+} increase, the egg cortex entered a relaxation phase, observed as slacking of the membrane on the surface of the glass coverslips. The AF488-phalloidin fluorescence intensity decreased to a level lower than those we had observed before the fertilization. Following this phase, we observed the second oscillation phase of [Ca^{2+}] (Dumollard and Sardet, 2001) and AF488-phalloidin–labeled F-actin (starting at around 11 min in Figure 3C) with intervals of 1–2 min. Similar to the first oscillation phase, [Ca^{2+}] and AF488-phalloidin oscillations were observed in a correlated manner. For each elevation of [Ca^{2+}], the increase of AF488-phalloidin fluorescence followed with a latent

time of approximately 30 s (Figure 3D). We observed that the increase of AF488-phalloidin fluorescence and the changes in the attached membrane area occurred almost synchronously without any detectable time differences.

Fluorescence polarization imaging of AF488-phalloidin–labeled F-actin revealed the transient alignment of F-actin at the cortex of fertilized *Ciona* eggs during the first ooplasmic segregation.

We used TIRFM-based instantaneous FluoPolScope (Mehta *et al.*, 2016) for exploring the spatial/temporal dynamics of F-actin alignments at the cell cortex of *Ciona* eggs, especially during the first phase of ooplasmic segregation. The instantaneous FluoPolScope detects the polarization orientation of fluorescence by acquiring four different polarized fluorescence images of the same object as shown in Supplemental Movie S4. In Figure 4A and Supplemental Movie S5 (left), we show a series of typical TIRFM images of *Ciona* eggs with AF488-phalloidin before ($t = –1'$) and after ($t = 3' –12'$) fertilization, until the time of the first cell division ($t = 44'$). In the fluorescence images (top photographs in Figure 4A), we observed speckle images of AF488-phalloidin bound to F-actin. We used speckles of AF488-phalloidin staining to compute the anisotropy of fluorescence (polarization factor) and the absolute polarization orientation of AF488 that report the degree of alignment and the net orientation of F-actin. We used the polarization factor of AF488 to remove the nonspecific staining signal of AF488 from further analysis, as the fluorescence from AF488-phalloidin was highly polarized only when it was bound to actin filaments. AF488-phalloidin bound to F-actin shows the polarized fluorescence orientation that is parallel to the length of F-actin (Mehta *et al.*, 2016). By observing the polarized fluorescence of AF488-phalloidin, we mapped the alignments of actin filaments at the cell cortex of *Ciona* eggs (bottom panel of Figure 4A and Supplemental Movie S5 [right]). As shown in the map of the fluorescence polarization orientation of AF488-phalloidin, we found highly aligned F-actin at the cell cortex at $t = 3'$ after fertilization. In this particular case, the orientation of F-actin alignment was around 150° in the laboratory coordinate system, as was observed in the peak of orientation histogram of the fluorescence polarization of AF488-phalloidin at $t = 3'$ (Figure 4B). It is worth noting that there was partially aligned F-actin in the same orientation before fertilization, as we see in the peak of the top histogram of fluorescence polarization orientation of AF488-phalloidin in Figure 4B. These observations suggested that there were preexisting, weakly aligned F-actin networks at the egg cortex before fertilization. The fertilization-induced signaling, which includes the elevation of [Ca^{2+}], triggered the increasing density of polymerized actin (as a fluorescence intensity increase of AF488-phalloidin in Figure 4A, top trace) and the facilitation of F-actin alignment (as an increase of polarization factor in Figure 4A, bottom trace) to the same orientation that had existed before the fertilization. The alignment of F-actin was observed for 9–10 min (Figure 4, A and C) after the fertilization and then disappeared along with the disassembly of F-actin (Figure 4A, $t = 12'$). Thus, the emergence of F-actin to the cell cortex was always associated with highly ordered alignment of F-actin, as we see in the fluorescence intensity and the polarization factor of AF488-phalloidin (Figure 4C). The polarization factor (anisotropy of polarized fluorescence, see *Materials and Methods* for further details) of F-actin alignment reached the highest value when the contractile ring for the first cell division was observed at around 44–45 min after fertilization (Figure 4A, $t = 44'$).

We tried to determine the orientation of observed F-actin alignments with respect to the A–V axis. Observation of microtubules by using CiEB1-mCherry (see *Materials and Methods* for details) allowed us to correlate the movement of sperm aster
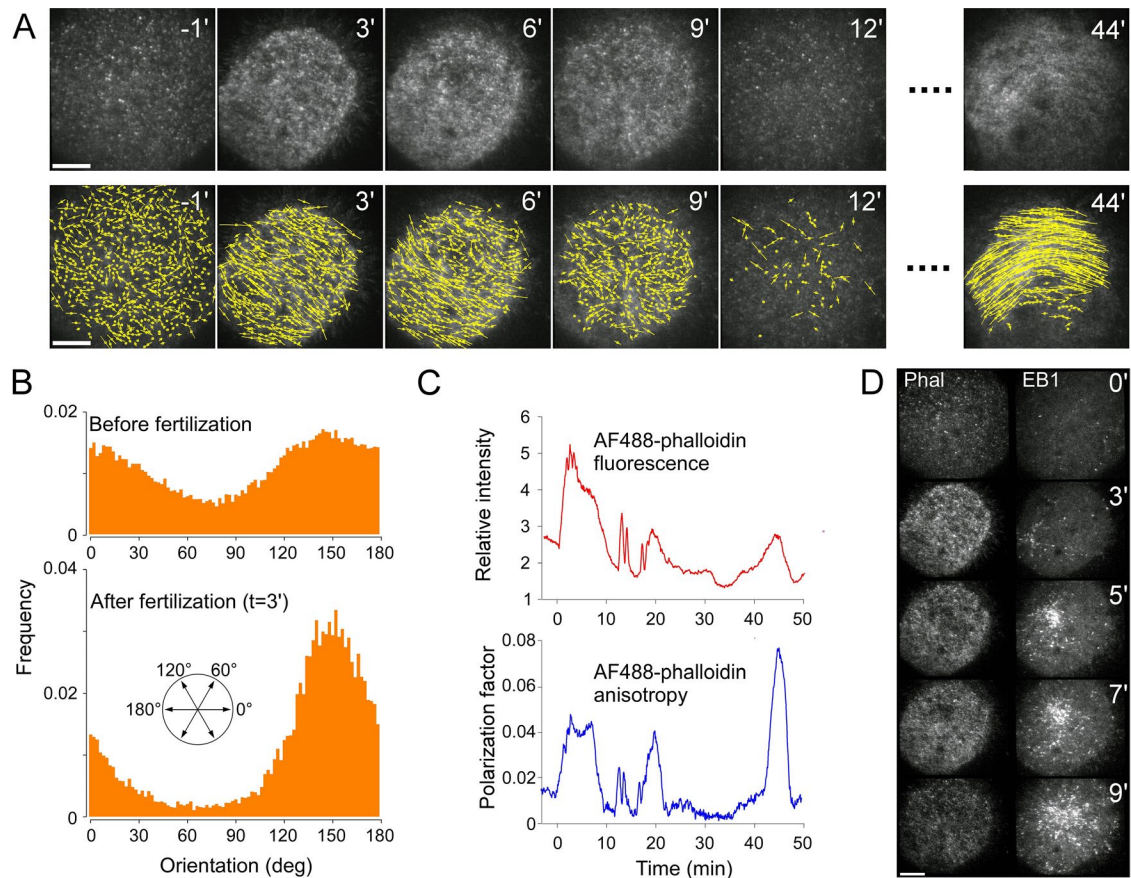
FIGURE 4: Transient F-actin alignment at the vegetal hemisphere during the first ooplasmic segregation of the *C. intestinalis* egg. (A) Time series of TIRFM images (top panel) and florescence polarization orientation maps (bottom panel) of a *Ciona* egg microinjected with AF488-phalloidin, before and after fertilization observed at the vegetal hemisphere, as we identified from the location of the sperm aster as shown in D. Positions of AF488-phalloidin particles bound to F-actin are shown as yellow dots. Orientation of the yellow bars represents the fluorescence polarization orientation of AF488, and the length of the bars represents the polarization factor. Bars, 10 μm. The numbers at the top right indicate the time (in minutes) before and after the onset of initial cortical contraction of the fertilized egg. (B) Histograms of the fluorescence polarization orientation of AF488-phalloidin in the *Ciona* egg cortex before (top) and after (bottom; 3 min after the onset of the first cortical contraction) fertilization. The frequency value represents the numbers of particles divided by the total number of particles analyzed. Orientations are shown in a laboratory coordinate system. (C) Time changes of the fluorescence intensity (top) and the fluorescence polarization of AF488-phalloidin observed at the cell cortex of the *Ciona* egg during fertilization. Time 0 represents the onset of initial cortical contraction of the fertilized egg. The relative intensity is derived from the averaged fluorescence intensity of measured area divided by the averaged background fluorescence intensity of the area outside the cell. For calculating the polarization factor, see *Materials and Methods*. (D) The change in the fluorescence intensity of AF488-phalloidin (Phal, left) and the movement of the sperm aster labeled with CiEB1-mCherry (EB1, right). The numbers at the top right indicate the time (in minutes) after the onset of initial cortical contraction. Bar, 10 μm.

with F-actin dynamics. As shown in Figure 4D and Supplemental Movie S6, the sperm aster, which was detected as a radially aligned CiEB1-mCherry bound to the vicinity of the plus end of microtubules, moved across the egg cortex during the cytoplasmic reorganization. Previous observations (Sardet *et al.*, 1989; Roegiers *et al.*, 1999; Ishii *et al.*, 2017) have revealed that after the initial phase of ooplasmic segregation, the sperm aster moves to the posterior-vegetal hemisphere along the A–V axis. The movement of the sperm aster in Figure 4D suggested that the alignments of F-actin that we observed in the vegetal hemisphere were normal to the A–V axis. To confirm whether the F-actin is consistently aligned perpendicular to the A–V axis in *Ciona* eggs, in the following section, we observed the alignment of F-actin at various locations where we could determine the A–V axis and the hemispheres of the observed area.

Locally distinct cortical F-actin alignments in fertilized *Ciona* eggs during the first ooplasmic segregation

On the basis of the correlative observation of the meiotic spindle (marker of animal pole), mitochondria (marker of vegetal hemisphere), and the Ca^{2+} wave propagations using SPIM (Figures 1 and 2), we found that the A–V axis could be estimated from the orientation of the sequestering waves. In 14 data sets among 22 trials of the instantaneous FluoPolScope imaging of *Ciona* eggs, we correlatively observed F-actin orientations, distribution of mitochondria and yolk granules, and Ca^{2+} waves before and after fertilization. We found there were two distinct F-actin alignment orientations at the cortex of fertilized *Ciona* eggs during the first phase of ooplasmic segregation. F-actin aligned normal to the A–V axis (Figure 5, C and D, and Supplemental Movie S7) at the vegetal hemisphere where we observed a dense distribution of
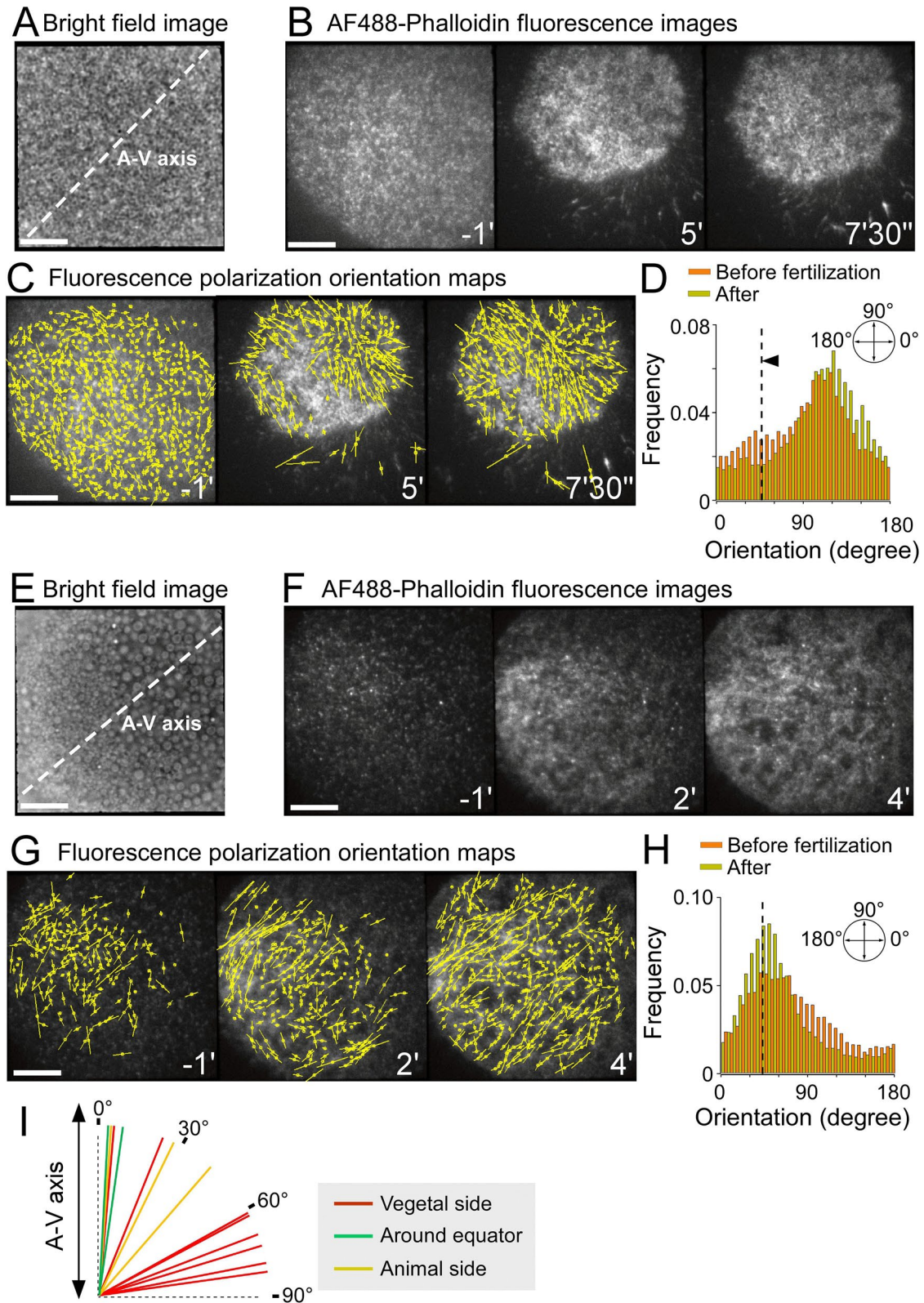
FIGURE 5: Locally distinct F-actin alignments in the *C. intestinalis* egg during the first ooplasmic segregation. (A) Bright field image of the vegetal hemisphere of the *Ciona* egg surface showing a uniform distribution of mitochondria. The A–V axis was determined by the propagation orientation of Ca^{2+}-sequestering waves. Bar, 10 µm. (B) Time series of TIRFM images of AF488-phalloidin at the cell cortex of *Ciona* observed in the same area as in A before (*t* = –1′) and after (*t* = 5′, 7′ 30″) the onset of fertilization-induced [Ca^{2+}] elevation. (C) Time series of the fluorescence polarization maps of AF488-phalloidin at the cell cortex of *Ciona* in the same area as observed in A and B before (*t* = –1′) and after (*t* = 5′, 7′ 30″) the onset of fertilization-induced Ca^{2+} elevation. (D) Histograms of the fluorescence polarization orientation of AF488-phalloidin in the *Ciona* egg before (orange) and 7 min 30 s after (yellowish green) the onset of

Prep no.	A: Types of cortical granules	B: F-actin alignment before fertilization (degrees)	C: F-actin alignment after fertilization (degrees)	D: First Ca²⁺ wave origin (degrees)	E: Ca²⁺-sequestering wave origin (degrees)	F: Pacemaker Ca²⁺ wave origin (degrees)	G: Minimum angle between C and E (degrees; 0°–90°)
1	All mitochondria	114	114	84	232	110	62
2	All mitochondria	9	12	224	81	254	69
3	All mitochondria	126	129	217	47	222	82
4	All mitochondria	42	150	73	223	267	73
5	All mitochondria	72	72	310	50	178	22
6	All mitochondria	78	78	33	73	40	5
7	Mitochondria dominant	48	52	323	131	227/67	79
8	Mitochondria dominant	108	117	65	56	255	61
9	Mitochondria dominant	93	96	143	152	323	56
10	Half mitochondria and half yolk granules	108	123	213	311	143	8
11	Half mitochondria and half yolk granules	Isotropic	120	139	297	120	3
12	Yolk granules dominant, some mitochondria	44	44	107	40	58/201	4
13	Yolk granules dominant, some mitochondria	Isotropic	81	289	220	38	41
14	All yolk granules	30	27	1	181	10/355	26

Analyses of F-actin alignments and A–V axes observed in the vegetal hemispheres (No. 1–No. 9, red columns), around the equator (No. 10–No.11, green columns), and in the animal hemisphere (No. 12–No. 14, yellow columns). Net F-actin alignments were determined from the orientation histograms of ensemble fluorescence polarization of AF488-phalloidin fluorescence. The orientation of the A–V axis for each egg was identified by the propagation direction of Ca²⁺-sequestering waves observed at the same area. See *Materials and Methods* for further details.

TABLE 1: F-actin alignments observed at various locations of cell cortex in *C. intestinalis* eggs.

submicron-diameter mitochondria (Figure 5A) with the transmitted light imaging. The time series of cortical F-actin alignment changes (Figure 5B) and the histograms of the polarization orientation of AF488-phalloidin–stained F-actin before and after the fertilization showed that in this particular case, the orientations of F-actin were around 126° (before fertilization) and 130° (after fertilization) in the laboratory coordinate system (Figure 5D). Based on the direction of the Ca²⁺-sequestering wave, the estimated A–V axis was 47°. In contrast, at the equatorial region where we observed the boundary of the region with submicron scale mitochondria and that with large (2–3-µm-diameter) yolk granules (Figure 5E), F-actin alignments before and after fertilization were near parallel to the A–V axis (Figure 5, F–H, and Supplemental Movie S8). We summarize the observed orientations of F-actin alignments with respect to the A–V axis at different locations of *Ciona* eggs in Figure 5I and Table 1.

fertilization-induced [Ca²⁺] elevation. Orientations are shown in a laboratory coordinate system. (E) Bright field image of the *Ciona* egg surface around the equator showing a boundary between the mitochondria-rich area and that rich in yolk granules. The A–V axis was determined by the propagation orientation of Ca²⁺-sequestering waves. Bar, 10 µm. (F) Time series of TIRFM images of AF488-phalloidin at the cell cortex of *Ciona* in the same area as observed in E before (*t* = –1′) and after (*t* = 2′, 4′) the onset of fertilization-induced [Ca²⁺] elevation. (G) Time series of fluorescence polarization maps of AF488-phalloidin at the cell cortex of *Ciona* in the same area as observed in E and F before (*t* = –1′) and after (*t* = 2′, 4′) the onset of fertilization-induced [Ca²⁺] elevation. (H) Histograms of the fluorescence polarization orientation of AF488-phalloidin in the *Ciona* egg before (orange) and 4 min after (yellowish green) the onset of fertilization-induced [Ca²⁺] elevation. Orientations are shown in a laboratory coordinate system. (I) Panel that summarizes the distribution of ensemble orientation of F-actin (estimated from the fluorescence polarization orientations of AF488-phalloidin) with respect to the estimated orientation of the A–V axis in *Ciona* eggs observed in 14 embryos in Table 1. The orientations of F-actin alignments observed at the vegetal hemisphere, around the equator, and at the animal hemisphere are shown in red, green, and yellow, respectively.

Thus, on the basis of our observations of F-actin orientation, distributions of mitochondria and yolk granules, and the Ca^{2+}-sequestering wave, we found that there was a local difference in the spatial organization of F-actin alignments with respect to the A–V axis at different locations of *Ciona* eggs during the initial phase of ooplasmic segregation. In 9 cases of 14, at the vegetal hemisphere, the observed F-actin alignments were close to the orientation perpendicular to the A–V axis. In the regions that we determined to be around the equator or animal hemisphere, F-actin alignments were mostly parallel along the A–V axis. We were not successful in imaging cortical F-actin orientation near the animal pole and vegetal pole, presumably because the attachment of egg membrane of these areas to the glass coverslip might interfere with the normal process of ooplasmic segregation.

DISCUSSION

Generation of cytoplasmic movements in fertilized *Ciona* eggs during actomyosin-driven ooplasmic segregation

By using SPIM, we imaged the dynamics of cytoplasmic reorganization in *Ciona* eggs after fertilization. The primary object of this imaging was to understand the mechanisms that cause cytoplasmic movements in fertilized *Ciona* eggs. Tracking of the movements of autofluorescent granules (mitochondria) at the vegetal hemisphere and microinjected fluorescent beads that spread over the whole cytoplasm of the eggs revealed that the onset of the first cytoplasmic reorganization was initiated by the cortical contraction at the myoplasm (Figure 1, C and E). The movement of myoplasm was followed by large cortical movements along the surface of the animal hemisphere, from the animal pole to the equator along the cell cortex (Figure 1, D and F). Our observations were fundamentally consistent with the hypothetical models proposed in previous studies (Jeffery and Meier, 1983; Jeffery, 1984; Sawada, 1983); the idea being that the first ooplasmic segregation is based on the contraction of the cell cortex at the vegetal hemisphere and the expansion of the cell cortex at the animal hemisphere.

Simultaneous monitoring of intracellular $[Ca^{2+}]$ and cytoplasmic movement revealed that, in fertilized *Ciona* eggs, cytoplasmic reorganization started after the completion of fertilization-induced $[Ca^{2+}]$ increase in the entire egg (Figures 1 and 3). In other words, the transient local difference of $[Ca^{2+}]$ during the propagation of the Ca^{2+} wave was not likely to be the main cause of local difference of actomyosin-driven cytoplasmic movements during the first ooplasmic segregation. These results might be inconsistent with the previous report using *Phallusia* eggs, that there was a spatial correlation between the sperm entry site and the location of a small protrusion near the vegetal pole (contraction pole) after the contraction of the vegetal hemisphere (Speksnijder *et al.*, 1990; Roegiers *et al.*, 1995). The previous observations of these authors suggested that the local difference of $[Ca^{2+}]$ during Ca^{2+} wave propagation might affect the actomyosin-driven deformation of the eggs in the vicinity of the vegetal pole. Rather, our observations indicated that the spatial dynamics of the first cytoplasmic reorganization in *Ciona* eggs after fertilization is controlled by the organization of the cytoskeletal architectures that have already been programmed during the spatial organization of oocyte during oogenesis.

Roles of Ca^{2+} waves for the establishment of cell polarity in fertilized *Ciona* eggs

We refined the Ca^{2+} waves in fertilized *Ciona* eggs by using SPIM, which allowed us to analyze the propagation of Ca^{2+} waves in three-dimensional (3D) space. By tracing the wavefront of these spatial $[Ca^{2+}]$ changes, we located the origins for each wave in 3D space.

On the basis of our analysis, we found that in *Ciona*, the origins of the first Ca^{2+} wave (fertilization-induced Ca^{2+} wave) were not limited in the vicinity of the animal pole (Figure 2D). A series of pacemaker waves that follow the first Ca^{2+} wave originated from a broad area within the vegetal hemisphere that corresponded to the location of the myoplasm. The vegetal origins of the pacemaker waves was generally consistent with previous reports that the ER and mitochondria-rich domains around the contraction pole were the origins of Ca^{2+} pacemaker waves (Speksnijder *et al.*, 1990; Roegiers *et al.*, 1995; Dumollard and Sardet, 2001).

We found a series of novel Ca^{2+}-sequestering waves that followed each rise of $[Ca^{2+}]$ (Figure 2B). Interestingly, based on our observations, the sequestering waves consistently originated from the animal pole (Figure 2D). The possible mechanisms for the propagating Ca^{2+} sequestration are unclear. Dumollard *et al.* (2003) found a Ca^{2+}-sequestering function of ascidian mitochondria, which was blocked by an application of inhibitors for the mitochondrial respiration function (Dumollard *et al.*, 2003). Similar to the simultaneous observations of $[Ca^{2+}]$ and mitochondrial flavoproteins (FAD^{++}) fluorescence changes in fertilized mouse eggs (Dumollard *et al.*, 2004), we found synchronous changes of $[Ca^{2+}]$ and autofluorescence observed through a 529/24 nm emission filter (Figure 2E), suggesting the involvement of mitochondria for the regulation of Ca^{2+} sequestration, in addition to the cytoplasmic $[Ca^{2+}]$ increase. At this point, we have no evidence to suggest the intracellular signals from the animal pole that mediates Ca^{2+} sequestration waves. Since the animal pole is the site for the egg nucleus, some signaling molecules of nuclear origin such as cdk1-cyclinB (Bischof *et al.*, 2017) might be involved in Ca^{2+} sequestration.

Local control of F-actin alignment as a possible mechanism for generating cytoplasmic movement during the first ooplasmic segregation of fertilized *Ciona* eggs

By using our own fluorescence polarization imaging method, we have found transient emergence and dissolution of highly aligned F-actin at the cortex of *Ciona* eggs right after fertilization (Figure 4A). The onset of the cortical F-actin alignments was consistent with that of the morphological changes of the eggs, as we observed with SPIM (Figure 1). On the basis of the correlative imaging of the propagation of Ca^{2+}-sequestering waves that propagated along the A–V axis, we found that the orientations of F-actin alignments at the vegetal hemisphere were almost normal to the A–V axis, whereas the orientations observed at the equator and animal hemisphere were closer to the A–V axis. To our knowledge, this is the first observation of F-actin alignments and their dynamics at the cortical domain of living eggs during fertilization. Interestingly, we observed weak alignments of cortical F-actin in unfertilized eggs, in which the orientations were similar to those observed after fertilization with respect to the A–V axis (Figures 4 and 5). These observations suggest that the locally distinct spatial organizations of the actin cytoskeleton at the cell cortex of the *Ciona* egg have been built during oogenesis. Thus, the basic alignments of actin filaments with respect to the A–V axis were established before fertilization and were kept unchanged even after fertilization. It is unclear how actin filaments are tangentially aligned with respect to the A–V axis during oogenesis.

We found that the presence of sperm aster changed the alignments of F-actin as we observed a less-dense and less-organized F-actin network at the location where the sperm aster was observed (Figure 5, A and D). The sperm aster and associated microtubule system alter the morphological change of the *Ciona* egg after fertilization (Sardet *et al.*, 1989; Roegiers *et al.*, 1999) and the following cytoplasmic rearrangement that reallocates myoplasm and
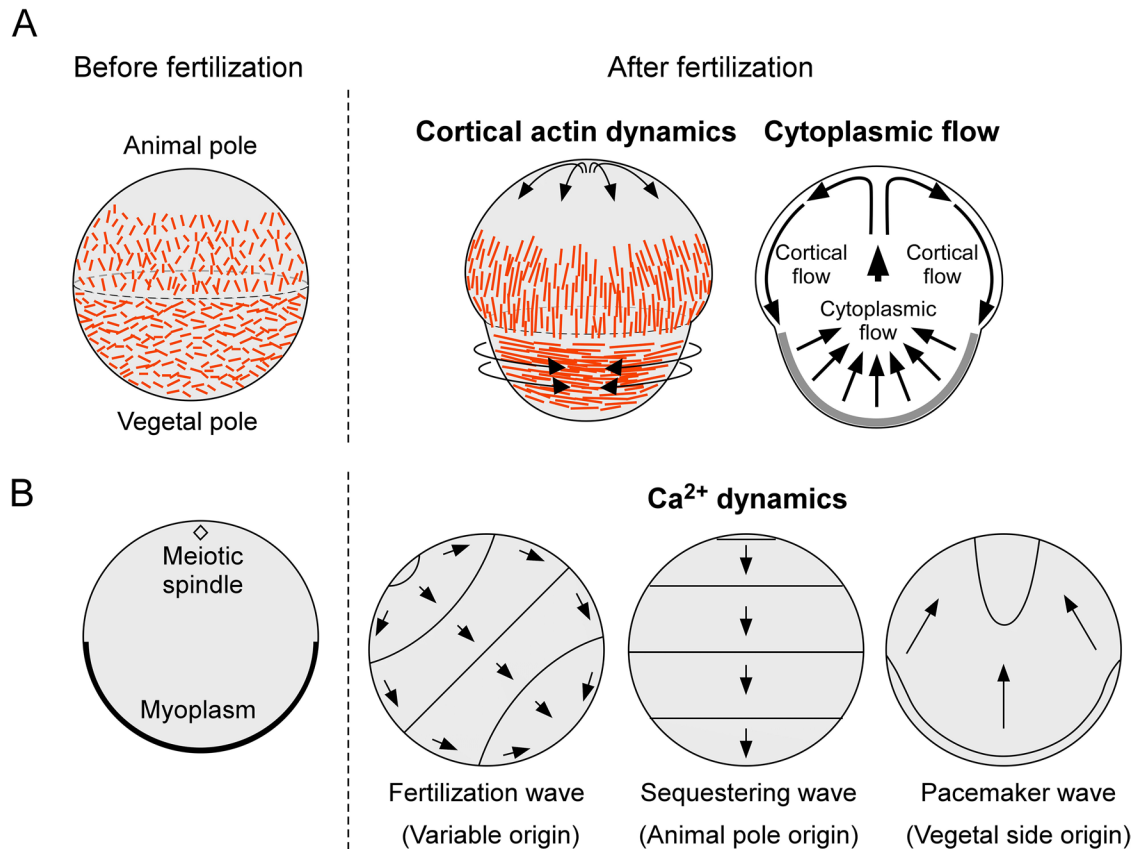
FIGURE 6: Local control of F-actin alignments for the first ooplasmic segregation. (A) Schematic drawings of cortical F-actin alignment changes before (left) and after (right) fertilization. The contraction of actomyosin at the vegetal hemisphere and resulting compression of vegetal cytoplasm leads to the cortical flow at the animal hemisphere that reallocates maternal factors in the cell cortex of the fertilized *C. intestinalis* egg (right). (B) Schematic drawings of intracellular Ca^{2+} waves in the fertilized *C. intestinalis* egg. Left: Scheme of the cross-section of a *Ciona* unfertilized egg showing the locations of the meiotic spindle and myoplasm. Right: Three patterns of the propagation of the Ca^{2+} wavefront across the egg. From left to right, fertilization-induced wave, sequestering wave, and pacemaker wave.

associated *postplasmic/PEM* RNAs to the future posterior side of the embryo (Sardet *et al.*, 2007; Makabe and Nishida, 2012). The roles of the sperm aster for organizing the architectures of cortical F-actin have been left as unanswered important questions for future studies.

On the basis of previously proposed models (Jeffery and Meier, 1983; Jeffery, 1984; Sawada, 1983) and our observations of F-actin alignments in *Ciona* eggs before and after fertilization, we propose a model including locally distinct F-actin alignments that might generate the force for cytoplasmic reorganization in fertilized egg (Figure 6). In this model we speculate that there are two orthogonal alignments of F-actin at the vegetal hemisphere and around the equatorial domain. At the vegetal hemisphere, actin filaments align latitudinal orientations that organize the constriction of the cup-shaped myoplasm along the latitudinal orientation. Like a contractile ring during cytokinesis, the contraction of laterally aligned F-actin bundles at the vegetal hemisphere squeezes the vegetal cytoplasm to the animal hemisphere. The movement of cytoplasm in the middle of the egg was somehow rectified near the animal pole and was converted to the stream that moves the cortex around the animal pole toward the equator along the longitudinal orientation. This cortical flow is associated with either passive or active alignment of actin filaments along the A–V axis. We postulate that the first cytoplasmic reorganization is thus accomplished through these cortical movements associated with the locally organized contractility of actomyosin at the cortex of ascidian eggs.

One of the challenges throughout our fluorescence polarization imaging of *Ciona* eggs was the moderate success rate when using the TIRFM system. The tight attachment of *Ciona* eggs to the glass coverslip (this is required for TIRFM imaging) interfered with the dynamic movement of the egg surface toward the vegetal pole after fertilization (Roegiers *et al.*, 1995), which caused abnormal deformation of the eggs before the first cell division. Instead of TIRFM, SPIM is a more favorable imaging system for *Ciona* eggs as it allows us to image suspended cells without tightly holding the cell surface. It is our future plan to develop SPIM with fluorescence polarization analysis, which will allow us to analyze the 3D orientations of F-actin and other protein assemblies in living cells/tissue and whole animals/plants in 3D space.

Bement, von Dassow, and their collaborators have reported an interesting observation of F-actin waves in the cell cortex of *Xenopus* and echinoderm embryonic cells in anaphase (Bement *et al.*, 2015). We have observed traveling waves of F-actin in *Ciona* eggs that were similar to those observed in *Xenopus* and echinoderms in size and speed, after the release of second polar body, which corresponds to anaphase before the cytokinesis of fertilized eggs (see Supplemental Movie S4 and S5; from 7 to 10 s in the movie). Our analysis of fluorescence polarization orientation revealed that there were alignments of F-actin in the waves.

Bement et al. (2015) proposed a model of F-actin and Rho as a reaction-diffusion system that represents excitable dynamics. Our unique molecular orientation approach will help in exploring the architectural dynamics of traveling F-actin waves in Xenopus eggs and eggs of other animal species.

MATERIALS AND METHODS
Request a protocol through Bio-protocol.

Collection of animals and the preparation of eggs
The ascidians Ciona intestinalis were collected from local yacht harbors near the Marine Biological Laboratory, Woods Hole, Massachusetts. The eggs collected from the oviduct of dissected Ciona were dechorionated with 1% sodium thioglycolate (Sigma Aldrich) and 0.05% protease (from Streptomyces griseus; Sigma Aldrich) dissolved in filtered natural seawater (FNSW) (Ishii et al., 2014).

SPIM imaging
We used a home-built a SPIM for monitoring the Ca²⁺ waves and the cytoplasmic movements of Ciona eggs after fertilization. Laser light sheet illumination was created by scanning beams from laser heads (488 nm, 20 mW, Sapphire, Coherent; 561 nm, 35 mW; 85-YCA; Melles Griot) with electromagnetic scanning mirrors (GVS202; Thorlabs). The scanned laser beams formed a light sheet at the specimen plane through an Olympus 4 × 0.25NA dry objective lens. The amplitude and the scan rate of the laser beams were controlled by a dual-channel function generator (Model 4087; BK precisions). Fluorescence emission was collected through a NA0.95, XLUMP-LANFL 20× Olympus water immersion lens. A green filter (529/24 nm; Semrock) was used for autofluorescence imaging, and a red filter (624/40 nm; Semrock) was used for Rhod-dextran or fluorescent bead imaging. Fluorescence images were taken with an EMCCD camera (iXon Ultra; Andor Technology). Collected images were fed into the computer (Precision 390; Dell) for further image analyses.

Instantaneous fluorescence polarization imaging
The instantaneous FluoPolScope (Mehta et al., 2016) was used to observe the orientation of local F-actin. Fluorescence polarization of AF488-phalloidin speckles reports the local orientation of F-actin (Mehta et al., 2016). The laser (DPSS laser BCD; 488 nm, 20 mW; Melles Griot) for excitation was circularly polarized by a quarter-wave plate (WPQ-4880–4M; Sigma-koki) and focused at the back focal plane (BFP) of the objective lens (PlanApo TIRFM 60× 1.49 N.A. oil; Nikon) of an inverted microscope (TE2000-E; Nikon). The circularly polarized laser beam was rotated in the BFP of the objective lens, with rotational frequency higher than 300 Hz to achieve isotropic illumination at the specimen plane. The beam was scanned along a circular annulus in the BFP using a pair of galvo-scanned mirrors (GVS202; Thorlabs). Fluorescence images were taken with an EMCCD camera (iXon+; Andor Technology). The pixel size of the EMCCD camera at the specimen plane was measured to be 180 nm. Emission filters we used were as follows: 529/24 nm transmission filter for AF488-phalloidin (Molecular Probes), 609/54 nm for Rhod-dextran (Molecular Probes) and for mCherry.

Preparation of eggs for fluorescence imaging
A solution of 5 μM AF488-phalloidin in distilled water (DW) was microinjected into the cytoplasm of dechorionated Ciona eggs for staining F-actin. The final concentration of AF488-phalloidin was estimated to be as low as 5–10 nM, based on the volume of microinjected AF488-phalloidin solution that was approximately from 1/1000 to 1/500 of the total cell volume of Ciona eggs. In general,

fluorescent phalloidin as low as 10 nM has little effect on the assembly/disassembly dynamics of actin in live cells (Tani et al., 2005; Yam et al., 2007; Mehta et al., 2016). For imaging spatial/temporal changes of intracellular Ca²⁺ concentration, we used Rhod-dextran. Rhod-dextran (50–500 μM) in distilled water was microinjected into the eggs. The final concentration of Rhod-dextran was estimated to be 50–500 nM, based on the volume of Rhod-dextran solution injected into the eggs. For imaging dynamics of microtubules in Ciona eggs, we constructed fluorescent protein fused microtubule plus-end binding protein EB1 from the Ciona EST clone (clone ID; cieg011b01) provided by Noriyuki Satoh, OIST, Japan, through the RIKEN BioResource Center (Satou et al., 2002). The open reading frame was amplified by PCR and inserted into the BmtI/BspEI site of the pRSETB-mCherry vector (Addgene plasmid 32382). The construct was transformed into Escherichia coli strain BL21(DE3). The CiEB1-mCherry proteins expressed with histidine tag were purified using a Ni-NTA column (GE Healthcare), and then the solvent was exchanged with DW by using a NAP-5 column (GE Healthcare). Purified CiEB1-mCherry in DW was microinjected into the dechorionated Ciona eggs together with AF488-phalloidin solution. The concentration of CiEB1-mCherry was estimated to be 20–40 nM, based on the volume of microinjected CiEB1-mCherry solution and the concentration of CiEB1-mCherry (18.2 μM). For tracking the movement of cytoplasmic reorganization processes, we microinjected 100-nm-diameter fluorescent polystyrene beads (Molecular Probes) to the eggs. Diluted solutions (1/100; in DW) of the original 2% suspension of the beads were microinjected to the eggs. The volume of microinjection was 1/1000 to 1/500 of the total volume of Ciona eggs.

Ciona eggs with microinjected fluorescence labels/indicators were mounted on washed glass coverslips (No. 1; Matsunami Glass). After letting the eggs settle on the glass, we observed the eggs with transmitted light to check the distribution of mitochondria and yolk granules. One 10⁶th dilution of sperm suspensions was applied for fertilizing dechorionated eggs. For TIRFM imaging, dechorionated eggs were tightly attached to the surface of the glass coverslips. However, in ascidian development, movement of the egg surface is essential for the normal development of the embryo (Roegiers et al., 1995). To minimize the interference of the tightly attached glass surface to the membrane dynamics of fertilized eggs, we added bovine serum albumin (BSA; Sigma Aldrich) to FNSW. We confirmed that in the seawater with 50 μg/ml BSA, approximately 67% of fertilized Ciona eggs showed normal first cell division. We set the first cell division as the benchmark to judge whether the normal development processes take place. The temperature of the imaging chamber was kept at 18°C throughout image acquisitions.

Image analyses
The polarization of a fluorescent particle was characterized by its degree of polarization, called the polarization factor (p), and the orientation (ϕ) of its maximum polarization. The particle intensity recorded in each quadrant is related to the average intensity across the four quadrants (I), the polarization factor, the orientation (ϕ), and the background intensity (I_{bg}) as follows:

$$I_n = I\left[1 + p\mathrm{Cos}\left(2n - 2\phi\right)\right] + I_{bg} \qquad (1)$$

where n= 0°, 45°, 90°, 135°.

Retrieval of the polarization orientation and the polarization factor of fluorescent objects are efficiently expressed in terms of the Stokes parameters of the polarization-resolved emission:

$$S_0 = 0.25\left(I_0 + I_{45} + I_{90} + I_{135}\right) - I_{bg} = I,\ S_1 = I_0 - I_{90},\ S_2 = I_{45} - I_{135} \qquad (2)$$

The above relationship can be written in matrix form as S = $M(I-I_{bg})$, where I = $[I_0, I_{45}, I_{90}, I_{135}]$T is the column vector of input intensities, S = $[S_0, S_1, S_2]$T is the column vector of Stokes parameters, and *M*, called the instrument matrix, is the matrix of coefficients that relate these two vectors according to Eq. 2. The matrix *M* in the above equation is replaced by the instrument matrix that is generated using the tangential polarizer as described previously (Mehta *et al.*, 2016).

The total particle intensity, polarization factor, and ensemble orientation were obtained from Stokes parameters as follows:

$$I_t = 4S_0 = 4I,\ p = (S_1^2 + S_2^2)^{1/2} / 2S_0,\ \phi = 0.5\tan^{-1}(S_2 / S_1) \qquad (3)$$

For other image analyses such as for quantitatively analyzing the propagation of Ca^{2+} waves, cytoplasmic flow, and the contraction of cortical membrane areas, we used Fiji, an open-source image processing package based on ImageJ (Schindelin *et al.*, 2012). For analyzing the propagation orientation of Ca^{2+}-sequestering waves at the narrow egg surface observed by TIRFM, the wavefront was manually determined and the line normal to the wavefront was defined as the orientation. The movement of cytoplasmic particles was tracked by using the MTrackJ plug-in (Meijering *et al.*, 2012).

REFERENCES
Altartouri B, Bidhendi AJ, Tani T, Suzuki J, Conrad C, Chebli Y, Liu N, Karunakaran C, Scarcelli G, Geitmann A (2019). Pectin chemistry and cellulose crystallinity govern pavement cell morphogenesis in a multi-step mechanism. Plant Physiol 181, 127–141.

Bement WM, Leda M, Moe AM, Kita AM, Larson ME, Golding AE, Pfeuti C, Su K-C, Miller AL, Goryachev AB, *et al.* (2015). Activator–inhibitor coupling between Rho signalling and actin assembly makes the cell cortex an excitable medium. Nat Cell Biol 17, 1471–1483.

Bischof J, Brand CA, Somogyi K, Májer I, Thome S, Mori M, Schwarz US, Lénárt P (2017). A cdk1 gradient guides surface contraction waves in oocytes. Nat Commun 8, 849.

Chiba S, Miki Y, Ashida K, Wada MR, Tanaka KJ, Shibata Y, Nakamori R, Nishikata T (1999). Interactions between cytoskeletal components during myoplasm rearrangement in ascidian eggs. Dev Growth Differ 41, 265–272.

Deno T (1987). Autonomous fluorescence of eggs of the ascidian Ciona intestinalis. J Exp Zool 241, 71–79.

Dumollard R, Hammar K, Porterfield M, Smith PJ, Cibert C, Rouvière C, Sardet C (2003). Mitochondrial respiration and Ca2+ waves are linked during fertilization and meiosis completion. Development 130, 683–692.

Dumollard R, Marangos P, Fitzharris G, Swann K, Duchen M, Carroll J (2004). Sperm-triggered [Ca2+] oscillations and Ca2+ homeostasis in the mouse egg have an absolute requirement for mitochondrial ATP production. Development 131, 3057–3067.

Dumollard R, Sardet C (2001). Three different calcium wave pacemakers in ascidian eggs. J Cell Sci 114, 2471–2481.

Dupont G, Dumollard R (2004). Simulation of calcium waves in ascidian eggs: insights into the origin of the pacemaker sites and the possible nature of the sperm factor. J Cell Sci 117, 4313–4323.

Goto T, Kanda K, Nishikata T (2019). Non-centrosomal microtubule structures regulated by egg activation signaling contribute to cytoplasmic and cortical reorganization in the ascidian egg. Dev Biol 448, 161–172.

Hiramoto Y (1976). Mechanical properties of sea urchin eggs III. Visco-elasticity of the cell surface. Dev Growth Differ 18, 377–586.

Huisken J, Stainier DYR (2009). Selective plane illumination microscopy techniques in developmental biology. Development 136, 1963–1975.

Ishii H, Goto T, Nishikata T (2017). Microtubule array observed in the posterior-vegetal cortex during cytoplasmic and cortical reorganization of the ascidian egg. Dev Growth Differ 59, 648–656.

Ishii H, Shirai T, Makino C, Nishikata T (2014). Mitochondrial inhibitor sodium azide inhibits the reorganization of mitochondria-rich cytoplasm and the establishment of the anteroposterior axis in ascidian embryo. Dev Growth Differ 56, 175–188.

Jeffery WR (1984). Pattern formation by ooplasmic segregation in ascidian eggs. Biol Bull 166, 277–298.

Jeffery WR, Meier S (1983). A yellow crescent cytoskeletal domain in ascidian eggs and its role in early development. Dev Biol 96, 125–143.

Lyczak R, Gomes J-E, Bowerman B (2002). Heads or tails: cell polarity and axis formation in the early Caenorhabditis elegans embryo. Dev Cell 3, 157–166.

Ma J, He F, Xie G, Deng W-M (2016). Maternal AP determinants in the Drosophila oocyte and embryo. Wiley Interdiscip Rev Dev Biol 5, 562–581.

Makabe KW, Nishida H (2012). Cytoplasmic localization and reorganization in ascidian eggs: role of postplasmic/PEM RNAs in axis formation and fate determination. Wiley Interdiscip Rev Dev Biol 1, 501–518.

McDougall A, Sardet C (1995). Function and characteristics of repetitive calcium waves associated with meiosis. Curr Biol 5, 318–328.

Mehta SB, McQuilken M, Riviere PJL, Occhipinti P, Verma A, Oldenbourg R, Gladfelter AS, Tani T (2016). Dissection of molecular assembly dynamics by tracking orientation and position of single molecules in live cells. Proc Natl Acad Sci USA 113, E6352–E6361.

Meijering E, Dzyubachyk O, Smal I (2012). Methods for cell and particle tracking. Methods Enzymol 504, 183–200.

Nakai N, Sato K, Tani T, Saito K, Sato F, Terada S (2019). Genetically encoded orientation probes for F-actin for fluorescence polarization microscopy. Microscopy 68, 359–368.

Nishida H (2005). Specification of embryonic axis and mosaic development in ascidians. Dev Dyn 233, 1177–1193.

Nishikata T, Goto T, Yagi H, Ishii H (2019). Massive cytoplasmic transport and microtubule organization in fertilized chordate eggs. Dev Biol 448, 154–160.

Nishikata T, Mita-Miyazawa I, Deno T, Satoh N (1987). Monoclonal antibodies against components of the myoplasm of eggs of the ascidian Ciona intestinalis partially block the development of muscle-specific acetylcholinesterase. Development 100, 577–586.

Nordenfelt P, Moore TI, Mehta SB, Kalappurakkal JM, Swaminathan V, Koga N, Lambert TJ, Baker D, Waters JC, Oldenbourg R, *et al.* (2017). Direction of actin flow dictates integrin LFA-1 orientation during leukocyte migration. Nat Commun 8, 2047.

Pelegri F (2003). Maternal factors in zebrafish development. Dev Dyn 228, 535–554.

Prodon F, Dru P, Roegiers F, Sardet C (2005). Polarity of the ascidian egg cortex and relocalization of cER and mRNAs in the early embryo. J Cell Sci 118, 2393–2404.

Prodon F, Yamada L, Shirae-Kurabayashi M, Nakamura Y, Sasakura Y (2007). Postplasmic/PEM RNAs: a class of localized maternal mRNAs with multiple roles in cell polarity and development in ascidian embryos. Dev Dyn 236, 1698–1715.

Reverberi G (1975). On some effects of cytochalasin B on the eggs and tadpoles of the ascidians. Acta Embryol Exp (Palermo) 1975, 137–158.

Roegiers F, Djediat C, Dumollard R, Rouviere C, Sardet C (1999). Phases of cytoplasmic and cortical reorganizations of the ascidian zygote between fertilization and first division. Development 126, 3101–3117.

Roegiers F, McDougall A, Sardet C (1995). The sperm entry point defines the orientation of the calcium-induced contraction wave that directs the first phase of cytoplasmic reorganization in the ascidian egg. Development 121, 3457–3466.

Sardet C (2003). Maternal mRNAs of PEM and macho 1, the ascidian muscle determinant, associate and move with a rough endoplasmic reticulum network in the egg cortex. Development 130, 5839–5849.

Sardet C, Paix A, Prodon F, Dru P, Chenevert J (2007). From oocyte to 16-cell stage: cytoplasmic and cortical reorganizations that pattern the ascidian embryo. Dev Dyn 236, 1716–1731.

Sardet C, Speksnijder J, Inoue S, Jaffe L (1989). Fertilization and ooplasmic movements in the ascidian egg. Development 105, 237–249.

Sardet C, Speksnijder J, Terasaki M, Chang P (1992). Polarity of the ascidian egg cortex before fertilization. Development 115, 221–237.

Satou Y, Yamada L, Mochizuki Y, Takatori N, Kawashima T, Sasaki A, Hamaguchi M, Awazu S, Yagi K, Sasakura Y, et al. (2002). A cDNA resource from the basal chordate Ciona intestinalis. Genesis 33, 153–154.

Sawada T (1983). How ooplasm segregates bipolarly in ascidian eggs. Bull Mar Biol Stn Asamushi 17, 123–140.

Sawada T, Osanai K (1984). Cortical contraction and ooplasmic movement in centrifuged or artificially constricted eggs of Ciona intestinalis. Wilhelm Roux Arch Dev Biol 193, 127–132.

Sawada T, Osanai K (1985). Distribution of actin filaments in fertilized egg of the ascidian Ciona intestinalis. Dev Biol 111, 260–265.

Sawada T, Schatten G (1988). Microtubules in ascidian eggs during meiosis, fertilization, and mitosis. Cell Motil Cytoskeleton 9, 219–230.

Schindelin J, Arganda-Carreras I, Frise E, Kaynig V, Longair M, Pietzsch T, Preibisch S, Rueden C, Saalfeld S, Schmid B, et al. (2012). Fiji: an open-source platform for biological-image analysis. Nat Methods 9, 676–682.

Speksnijder JE, Sardet C, Jaffe LF (1990). The activation wave of calcium in the ascidian egg and its role in ooplasmic segregation. J Cell Biol 110, 1589–1598.

Swaminathan V, Kalappurakkal JM, Mehta SB, Nordenfelt P, Moore TI, Koga N, Baker DA, Oldenbourg R, Tani T, Mayor S, et al. (2017). Actin retrograde flow actively aligns and orients ligand-engaged integrins in focal adhesions. Proc Natl Acad Sci USA 114, 10648–10653.

Takatori N, Oonuma K, Nishida H, Saiga H (2015). Polarization of PI3K activity initiated by ooplasmic segregation guides nuclear migration in the mesendoderm. Dev Cell 35, 333–343.

Tani T, Miyamoto Y, Fujimori KE, Taguchi T, Yanagida T, Sako Y, Harada Y (2005). Trafficking of a ligand-receptor complex on the growth cones as an essential step for the uptake of nerve growth factor at the distal end of the axon: a single-molecule analysis. J Neurosci 25, 2181–2191.

Weaver C (2004). Move it or lose it: axis specification in Xenopus. Development 131, 3491–3499.

Yam PT, Wilson CA, Ji L, Hebert B, Barnhart EL, Dye NA, Wiseman PW, Danuser G, Theriot JA (2007). Actin–myosin network reorganization breaks symmetry at the cell rear to spontaneously initiate polarized cell motility. J Cell Biol 178, 1207–1221.

Zalokar M (1974). Effect of colchicine and cytochalasin B on ooplasmic segregation of ascidian eggs. Wilhelm Roux Arch Entwickl Mech Org 175, 243–248.